Kim et al. *NPG Asia Materials* (2022) 14:67
https://doi.org/10.1038/s41427-022-00415-2

NPG Asia Materials

ARTICLE Open Access

Sign-tunable anisotropic magnetoresistance and electrically detectable dual magnetic phases in a helical antiferromagnet

Jong Hyuk Kim[1], Hyun Jun Shin[1], Mi Kyung Kim[1], Jae Min Hong[1], Ki Won Jeong[1], Jin Seok Kim[1], Kyungsun Moon[1], Nara Lee[1] and Young Jai Choi[1]

Abstract

Emerging from competing exchange interactions, the helimagnetic order describes a noncollinear spin texture of antiferromagnets. Although collinear antiferromagnets act as the elemental building blocks of antiferromagnetic (AFM) spintronics, until now, the potential of implementing spintronic functionality in noncollinear antiferromagnets has not been clarified. Here, we propose an AFM helimagnet of $EuCo_2As_2$ as a novel single-phase spintronic material that exhibits a remarkable sign reversal of anisotropic magnetoresistance (AMR). The contrast in the AMR arises from two electrically distinctive magnetic phases with spin reorientation that is driven by the magnetic field prevailing in the easy plane, which converts the AMR from positive to negative. Furthermore, based on an easy-plane anisotropic spin model, we theoretically identified various AFM memory states associated with the evolution of the spin structure under magnetic fields. The results revealed the potential of noncollinear antiferromagnets for application in the development of spintronic devices.

Introduction

The advancements in the research of antiferromagnetic (AFM) spintronics have opened new avenues for spin-based devices[1–3]. Generally, collinear antiferromagnets are utilized as the elementary basis for spintronic functionalities[4–6]. However, recent examinations of intriguing and unexpected physical phenomena in noncollinear antiferromagnets have expanded the scope of potential materials for exploiting AFM spintronics[2,7–9]. In particular, a large anomalous Hall effect was observed in noncollinear antiferromagnets, despite the vanishingly small magnitude of magnetization[7,10]. The Hall effect originates from the Berry curvature associated with topologically nontrivial spin textures[11–13]. Although its experimental observation is challenging, recent magnetic imaging techniques such as single spin relaxometry and scanning thermal gradient microscopy can be used for imaging noncollinear AFM textures and domain structures[14–16].

The ability to control and detect AFM memory states is imperative for AFM spintronics, and accordingly, magnetocrystalline anisotropy has been exploited as a generic foundation for manipulating AFM states[17,18]. As controlled anisotropy provides an exceptional opportunity for extensive spintronic applications[17,19], anisotropic magnetoresistance (AMR) has been adopted to detect the various resistive states associated with crystal axes[20–23]. Nonetheless, in several cases, an intricate stacking geometry with additional reference layers is required to achieve unified spintronic functionality[24,25].

Helimagnets exhibit a prototypical noncollinear spin structure in which the spin direction is spatially rotated in the plane, whereas the rotation axis is parallel to the propagation direction[26]. In principle, helimagnets are noncollinear antiferromagnets that correspond to the zero

Correspondence: Nara Lee (eland@yonsei.ac.kr) or Young Jai Choi (phylove@yonsei.ac.kr)
[1]Department of Physics, Yonsei University, Seoul 03722, Korea
These authors contributed equally: Jong Hyuk Kim, Hyun Jun Shin, Mi Kyung Kim

net moment inherent in rotating spins. Thus, helimagnets offer the same advantages as antiferromagnets, such as the absence of a stray field and the features of intrinsically fast spin dynamics[27–29]. Despite these merits, a crucial problem with noncollinear AFM spintronics is the establishment of controllable factors and mechanisms for the anisotropy of noncollinear spin configurations. Specifically, the lack of a comprehensive understanding of AMR affects its control and application in spintronic devices. In this research, we demonstrate that the helix-to-fan transition induces a sign reversal of the AMR in a helical antiferromagnet of $EuCo_2As_2$ (ECA). Moreover, we verified the electrically discernible dual magnetic phases producing the alterable sign of the AFM memory state through both experimental and theoretical methods. In addition, we identified diverse AFM memory states relevant to the development of the spin structure under magnetic fields, which facilitates AFM spintronics based on noncollinear antiferromagnets.

Materials and methods

Sample preparation

The ECA single crystals were grown following the flux method with Sn flux[30]. Eu (99.9%, Alfa Aesar), Co (99.5%, Alfa Aesar), As (99.999%, Sigma Aldrich), and Sn (99.995%, Alfa Aesar) were mixed at a 1.05:2:2:15 molar ratio of Eu:Co:As:Sn. The mixture was placed in an alumina crucible sealed in an air-evacuated quartz tube. The quartz tube was placed in a high-temperature furnace at 1050 °C for 20 h and thereafter gradually cooled to 600 °C at a rate of 3.75 °C/h. At 600 °C, the incorporation of the remaining Sn flux in the crystals was prevented by using a centrifuge composed of stainless steel, while the quartz tube was cooled to room temperature. Ultimately, we obtained crystals with typical dimensions of $1.5 \times 1.5 \times 0.1\ mm^3$.

Scanning transmission electron microscopy (STEM) measurement

We prepared ECA samples with a cutting plane perpendicular to the *a*-axis utilizing a dual-beam focused ion beam system (Helios 650, FEI). Along the cutting plane, the images presented a well-discernible atomic structure. To minimize any damage to the sample, the acceleration voltage conditions were gradually reduced from 30 to 2 keV. In addition, dark-field images were obtained using STEM (JEM-ARM200F, JEOL Ltd, Japan) at 200 keV with a Cs-corrector (CESCOR, CEOS GmbH, Germany) and a cold field-emission gun. The size of the electron probe was 83 pm, and the range of the high-angle annular dark-field detector angle was varied from 90 to 370 mrad.

Magnetic and transport property measurements

The dependence of magnetization on temperature and magnetic field was determined with the magnetic fields along the *a*- and *c*-axes using a vibrating sample magnetometer module in a physical property measurement system (PPMS, Quantum Design, Inc.). The electric transport measurements were performed using the conventional four-probe method in the PPMS. The AMR was measured by rotating the magnetic field in the *ac* plane in a PPMS equipped with a single-axis rotator.

Theoretical calculations

The easy-plane anisotropic spin model can be expressed as

$$\mathcal{H}/N = J_1\sum_{i=1}^{5}\vec{S}_i\cdot\vec{S}_{i+1} + J_2\sum_{i=1}^{5}\vec{S}_i\cdot\vec{S}_{i+2} - g\mu_B\vec{H}\cdot\sum_{i=1}^{5}\vec{S}_i + K_\theta\sum_{i=1}^{5}cos^2\theta_i - K_5S\frac{\left(1+\sin^4\theta\right)}{2}\sum_{i=1}^{5}\cos 5\varphi_i$$

where N denotes the number of Eu^{2+} moments in a single layer; J_1 and J_2 represent the AFM coupling strength between the Eu^{2+} moments of the two nearest layers and the next-nearest layers, respectively; $S = 7/2$ for Eu^{2+} ions; $g = 2$; and K_θ denotes the magnetocrystalline anisotropy constant[31]. We considered the helical spin structure of the ECA as commensurate ($k = 0.8$) for the convenience of calculation and thus included only five layers with the periodic boundary condition. The first and second terms indicate the competing exchange interactions for an AFM helical state. The third term designates the Zeeman energy, where the magnetic field $\vec{H}$ is situated on the *ac* plane, forming an angle θ with the *c*-axis. The fourth term denotes the easy-plane magnetocrystalline anisotropy energy that favors the planar spin orientation. The fifth term reflects that we are working with a three-dimensional system, considering the ferromagnetic interactions within a given layer as a mean-field term. For the helical AFM state, where $\varphi = \frac{4}{5}\pi$, i.e., $J_2 = 0.31J_1$, we estimated the following parameters by fitting the theoretical results of anisotropic magnetization to the experimental data: $g\mu_B H_m/J_1S = 1.18$, $K_\theta = 0.35J_1S^2$, and $K_5 = 0.022J_1S$, where H_m indicates the occurrence of the helix-to-fan transition. Using $H_m = 4.7$ T for the ECA at 2 K, J_1S^2 and K_θ can be evaluated as 5.45×10^6 and $1.96 \times 10^6\ J/m^3$, respectively.

Results

Structure and properties of helical ECA antiferromagnets

A two-dimensional (2D) layered ECA helimagnet forms a body-centered tetragonal structure (I4/mmm space group)[30]. The crystal exhibits a strong 2D nature that enables it to be mechanically exfoliated. By composition, it consists of two Co_2As_2 layers on opposite sides of a unit cell, separated by a magnetic Eu layer, as depicted in Fig. 1a[32]. As crystal quality is an essential aspect for investigating distinguished anisotropy, it was reviewed

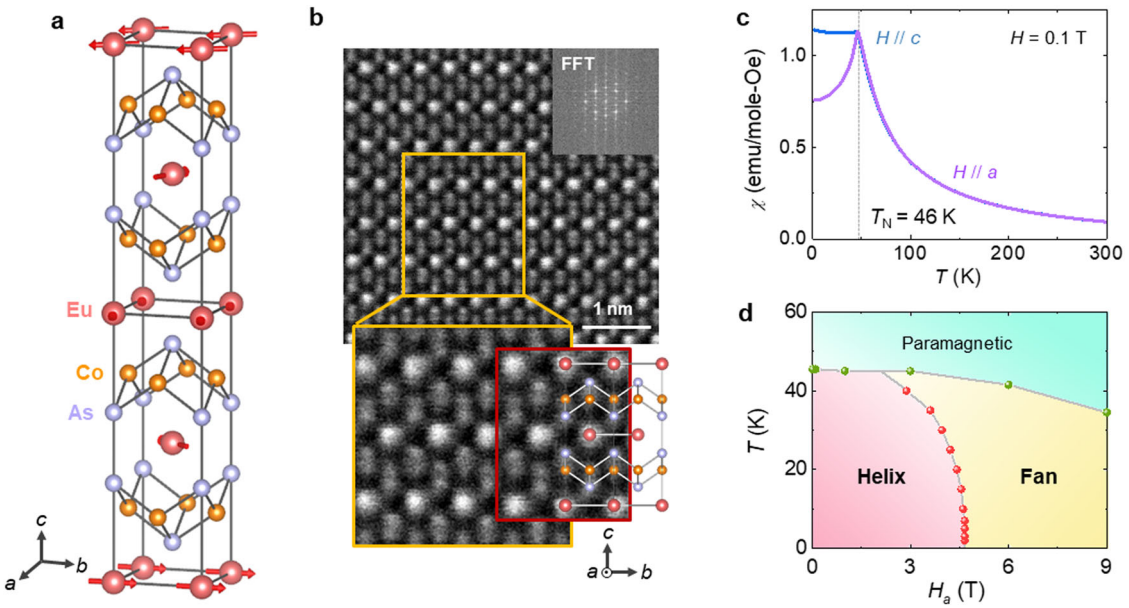

Fig. 1 Structure and magnetic susceptibility of ECA. a Crystal and spin structures of ECA. Red, orange, and light purple spheres denote Eu, Co, and As atoms, respectively. The red arrow on each Eu atom indicates the individual spin direction. Competing exchange interactions form the helical AFM order along the *c*-axis with $\boldsymbol{k} = (0, 0, 0.79)$. **b** Dark-field STEM images in the *bc* plane. Inset: diffraction pattern obtained from FFT. **c** Temperature (*T*) dependence of magnetic susceptibility $\chi = M/H$, measured upon warming at $H = 0.1$ T after zero-field cooling for the *a*- and *c*-axes. Vertical gray line specifies Néel *T*, $T_N = 46$ K. **d** *H*–*T* phase diagram for *H* // *a*. Red dots distinguish the phase boundary between helix and fan phases, estimated by isothermal magnetization. Green dots indicate the Néel *T* at each *H*.

using the single-crystal X-ray diffraction technique. The analyses revealed the crystals as a single phase with high quality (refer to Supplementary S1). The magnetic moments of the Eu^{2+} ions ($S = 7/2$ and $L = 0$) were helically ordered, whereas those of the Co ions were paramagnetic and not relevant to the magnetic ordering[30,33]. The direction of the net moment in the Eu layer rotates in the *ab* plane and propagates along the *c*-axis (Fig. 1a). In general, the pitch of the helix was incommensurate with the lattice parameter, and thus, no two layers exhibited the same directions of the net moments[34]. In the ECA, a slightly incommensurate helimagnetic order with a propagation vector $\boldsymbol{k} = (0, 0, 0.79)$ has been observed via neutron diffraction[32], which indicates that the AFM interaction between the adjacent layers is perturbed by an additional AFM interaction acting between the second-neighbor layers[31]. Accordingly, STEM was utilized to visualize the structural units of alternately arranged Eu and Co_2As_2 layers (Fig. 1b). The STEM image with lower magnification indicates that all the layers were regularly aligned. The lattice constants were obtained using fast Fourier transformation (FFT) from the STEM data with $a = 0.402$ nm and $c = 1.150$ nm, similar to the results of previous reports[30,32].

The helical AFM order emerges at $T_N = 46$ K, as evident from the temperature (*T*) dependence of the magnetic susceptibility defined by the magnetization (*M*) divided by the magnetic field (*H*), $\chi = M/H$, measured at $H = 0.1$ T (Fig. 1c). The χ curves below T_N for *H* along the *a*- and *c*-axes (H_a and H_c) indicate an anisotropic nature. The rapid decrease in χ for H_a below T_N is consistent with the alignment of the magnetic moments of Eu ions along the *ab* plane, as previously verified *via* neutron diffraction and nuclear magnetic resonance experiments[32,33]. We observed metallic behavior with a distinct anomaly at T_N, as shown by the variations in resistivity with *T* (refer to Supplementary Fig. S2). Therefore, an indirect Ruderman–Kittel–Kasuya–Yosida (RKKY) exchange interaction between the Eu^{2+} spins mediated by the spins of conduction electrons can be expected[35]. The phase diagram of the *T* and H_a dependences of the magnetic properties is illustrated in Fig. 1d, which clarifies the phase boundary between the helix and fan structures.

Electrically distinguishable dual magnetic phases and magnetoresistance anisotropy

In an antiferromagnet, an adequately strong *H* along a magnetic easy-axis often generates a magnetic phase transition through spin reorientation, such as a spin-flop or spin-flip transition[30,36]. Phase conversion occurs with marked anomalies in the physical properties and stabilizes the flopped or flipped state. We observed a similar magnetic phase transition in the helimagnetic ECA. At 2 K, M_a (*M* along the *a*-axis) abruptly increases at $H_m = 4.7$ T,

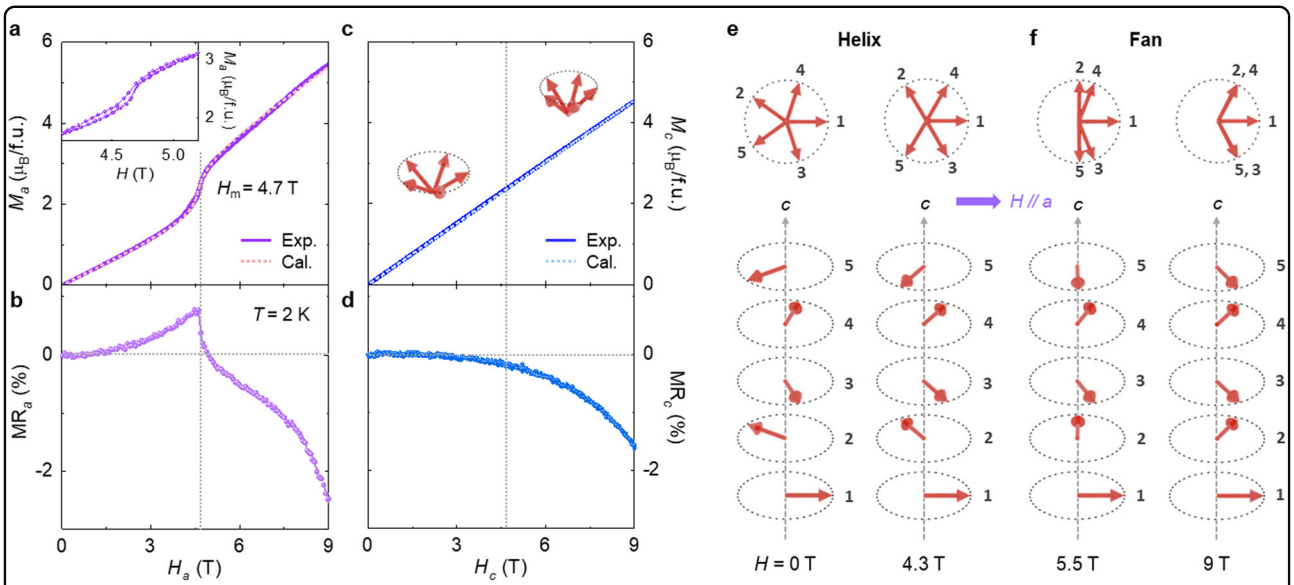

Fig. 2 Magnetization and magnetoresistance anisotropies. a Isothermal magnetization along the *a*-axis (M_a) at $T = 2$ K. Experimental and calculated data are plotted as solid and dotted curves, respectively. The vertical gray line denotes the occurrence of the helix-to-fan transition. $H_m = 4.7$ T. Inset: magnified view of M_a to elucidate the magnetic hysteretic behavior. **b** Isothermal magnetoresistance, MR (%), along the *a*-axis (MR$_a$) at $T = 2$ K. **c** Isothermal magnetization along the *c*-axis (M_c) at $T = 2$ K. Inset: schematics of canted helical-spin structures at H_c, in which the beginnings of arrows in layers indicate net magnetic moments placed together at a single point. **d** Isothermal magnetoresistance, MR (%), along the *c*-axis (MR$_c$) at $T = 2$ K. **e** Estimated spin configurations of helix states formed below the phase transition ($H < H_m$). **f** Estimated spin configurations of fan states formed above the transition ($H > H_m$). The red arrow indicates the net magnetic moment in each Eu layer numbered from 1 to 5 along the *c*-axis.

thereby indicating a helix-to-fan transition[30]. The similarity of this transition to spin-flops is signified by the extrapolation of the linear slope above H_m that merges at the origin (Fig. 2a). H_m was determined from the peak in the derivative of M_a. As displayed in the inset of Fig. 2a, slight magnetic hysteresis is observed to arise from the first-order characteristic of this transition (refer to Supplementary Information S2). Across the phase transition, a fan structure emerges in which the net magnetic moments spatially oscillate along the propagation vector[30,31,35]. In contrast, M_c (M along the *c*-axis) at 2 K displays a linear increase associated with the gradual canting of the net moments (Fig. 2c). The slope of M_a is smaller than that of M_c below H_m and becomes larger in magnetic fields greater than H_m. Therefore, the value of M_a exceeds M_c at H_m.

An easy-plane anisotropic spin model was adopted to investigate the evolution of the helix-to-fan phase. The model Hamiltonian comprises the competing exchange interactions, Zeeman energy, magnetocrystalline anisotropy, and mean-field terms (refer to Methods and Supplementary Information S2 for details). Additionally, the commensurate helical spin structure was considered for convenience of calculation. The relative angle of the two moments between the most proximate layers at zero H was $\varphi = \frac{4}{5}\pi$, corresponding to $j_2 = 0.31J_1$, because the relative angle of the two spins for a helical order can be expressed as $\varphi = \cos^{-1}\left(-\frac{J_1}{4J_2}\right)$[31,34]. As the planar spin rotation is explicitly disintegrated with the application of H_a, the order parameter of the helical state can be expressed as $\sum_{i=1}^{5}\cos 5\varphi_i$. Thus, the ferromagnetic interactions within a given layer can be treated by adding a mean-field term. The estimated M_a and M_c values obtained from the experimental data are represented as dotted curves in Fig. 2a, c. The well-matched fitting in the absence of a fourfold rotational magnetocrystalline anisotropy in the *ab* plane implies the formation of helical spins that are independent of the planar crystalline axes in the ECA. Moreover, the theoretical estimation directly generated the spin configurations pertaining to the helix and fan phases, as illustrated in Fig. 2e, f. In the helix phase, the orientations of the net moments continually turned in the H direction as H_a increased. Greater than H_m, spin reorientation occurred in such a manner that the moments acting farther from the H direction tended to be perpendicular. A further increase in H_a generated an additional canting of the magnetic moments.

The influence of anisotropic M on transport was examined based on the magnetoresistance, $MR = \frac{R(H)-R(0)}{R(0)}$, for both the *a*- and *c*-axes (MR$_a$ and MR$_c$). The increase in M_a with increasing H below H_m (Fig. 2a)

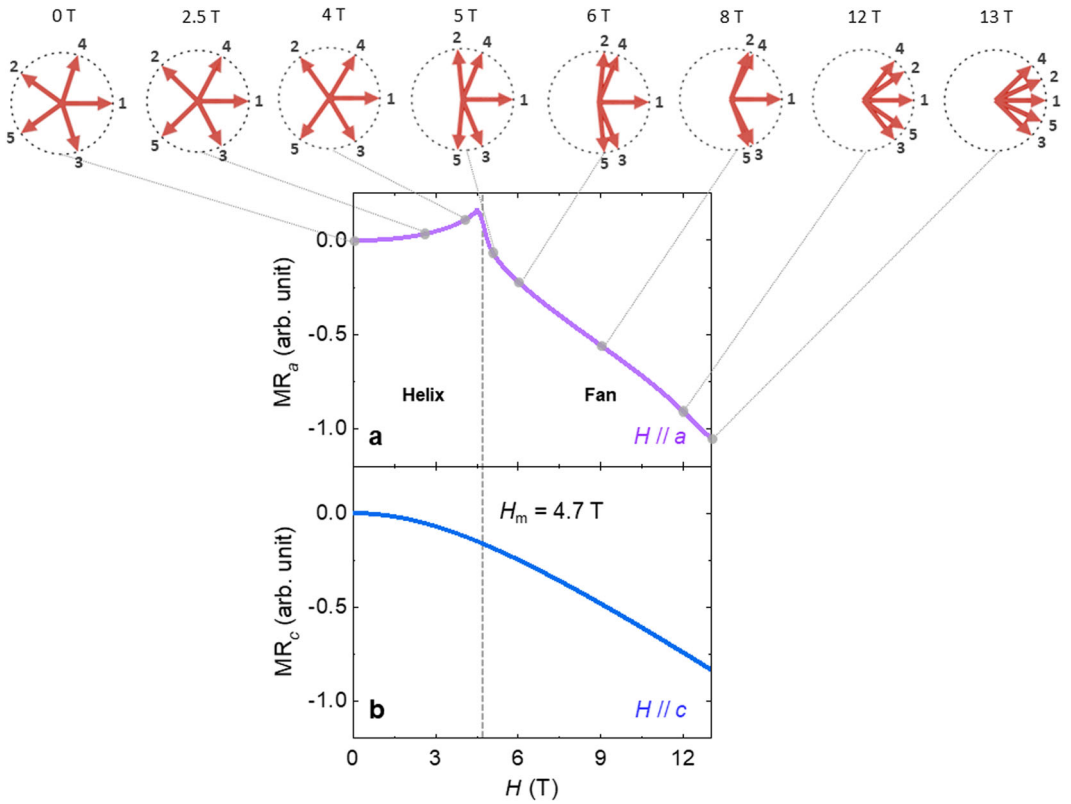

Fig. 3 Calculated magnetoresistance anisotropy. a Theoretically estimated isothermal magnetoresistance, MR, along the *a*-axis (MR$_a$). Schematics of net magnetic moment configurations corresponding to multiple MR$_a$ states at various values of H_a. **b** Theoretically estimated isothermal magnetoresistance, MR, along the *c*-axis (MR$_c$).

indicates a partial and gradual alignment of the magnetic moments in the H direction. The average net magnetic moment along the H direction disrupts the equally distributed angles between the moments in the layers (Fig. 2e). The spin configuration away from the helix state increases the resistance, i.e., a positive MR$_a$ (Fig. 2b). With a further increase in H, MR$_a$ exhibits an abrupt reduction with the maximum slope at H_m and becomes negative. The spin-reorientation-driven switching from positive to negative MR$_a$ is consistent with the crossing behavior of M_a. In the high-H regime, MR$_a$ decreases faster with the additional canting of the moments toward the flipped state (Fig. 2f). In contrast, MR$_c$ decreases with increasing H (Fig. 2d). This intimate correlation between the M and MR plots suggests that the magnetic order governs the magnetotransport and its anisotropy. As T increases, H_m decreases, and the shape of the anomaly is broadened, as displayed in the anisotropic M and MR plots at various T values in Supplementary Fig. S6.

To theoretically probe the magnetotransport property, we propose that the interlayer hopping amplitude can be expressed by $t_{i,i+1} = t_0 + t_s|<\hat{n}_i|\hat{n}_{i+1}>|$ $(i = 1–5)$ with the periodic boundary condition, where t_0 and t_s indicate the spin-independent and spin-dependent parts, respectively. Here, $|<\hat{n}_i|\hat{n}_{i+1}>|$denotes the overlap integral between the two spinors. Each spinor aligns with the direction of the net magnetic moment in each layer. The overlapping integral is given by $\cos\frac{\gamma}{2}$, where γ denotes the relative angle between the two spinors. For the MR calculations, the conductance (σ) of the system was assumed to be proportional to the geometric mean of multiple hopping amplitudes through the layers as $\sigma \propto \left(\prod_{i=1}^{5} t_{i,i+1}\right)^{\frac{1}{5}}$, where the geometric mean effectively presumes the average of the product $\prod_{i=1}^{5} t_{i,i+1}$. According to the definition of MR and $R = 1/\sigma$, MR is proportional to $\sigma(\sigma) - \sigma(H)$. Upon setting $t_0/t_s = 0.2$, the highly anisotropic trend between MR$_a$ and MR$_c$ is moderately described by the purely spintronic consideration of σ (Fig. 3a, b). This is because of the $L = 0$ condition for the ground state of the Eu^{2+} ions[34]. The MR response to an applied H_a prominently distinguished two distinct magnetic phases. In the helix phase, the increased γ for certain adjacent layers at H_a below H_m contributes more to σ as it reduces, thereby

inducing positive MR_a. For small H_a, one can explicitly prove that σ decreases with H_a. In this regime, an interlayer hopping amplitude can be approximately expressed as $t_{i,i+1} \cong \bar{t}e^{-\alpha\epsilon_i/2-\beta\epsilon_i^2/4}$, where $\epsilon_i = \varphi_{i+1} - \varphi_i - \frac{4\pi}{5}$ represents the small deviation of the relative spin orientation $\varphi_{i+1}-\varphi_i$ from the average value, $\bar{t} = t_0 + t_s cos\frac{2\pi}{5}$, $\alpha = t_s sin\frac{2\pi}{5}/\bar{t}$, and $\beta = t_s\left(t_s + t_0 cos\frac{2\pi}{5}\right)/2\bar{t}^2$. As $\sum_{i=1}^{5}\epsilon_i = 0$, $\sigma \propto \left(\prod_{i=1}^{5} t_{i,i+1}\right)^{\frac{1}{5}} = \bar{t}e^{-\beta\sum_{i=1}^{5}\epsilon_i^2/20} < \bar{t}$. Therefore, σ reduces for small H_a. In the fan phase, γ continuously decreases with a further increase in H_a by approaching the completely spin-aligned state along the magnetic field direction, which enhances σ and diminishes MR_a. Various AFM memory states relevant to the various spin configurations under an external H_a were theoretically identified, as depicted in Fig. 3a.

Spin-reorientation-driven reversal of anisotropic magnetoresistance

A peculiar spintronic characteristic of a noncollinear AFM ECA is presented by angle-dependent magnetotransport. The results of the AMR, defined as $\frac{R(\theta)-R(0)}{R(0)}$, are depicted in Fig. 4a, b. As indicated in the geometry of the AMR measurement in Fig. 4a, H is continually rotated perpendicular to the current, excluding the extrinsic Lorentzian MR effect. At $H < H_m$, ab-planar helix formation facilitates twofold rotational symmetry. The AMR is maximized at $\theta = 90°$ and 270° (Fig. 4a) owing to the positive value of MR_a, which gradually increases with H (Fig. 2b). At H values slightly exceeding H_m, the AMR near $\theta = 90°$ and 270° starts to partially reverse, which is observed as a dip in Fig. 4a. A further increase in H results in a complete reversal of the AMR. The AMR contour map (Fig. 4b) demonstrates the sign-tunable AMR upon crossing H_m. The detailed influence of increasing T on the AMR is plotted in the contour maps of Supplementary Fig. S7. The overall trend of AMR development under the applied H was reproduced using theoretical calculations, as portrayed in Fig. 4c, d. The contrast emerging from the reversal behavior of the AMR effect reflects the intrinsic bulk properties and clarifies the different magnetotransport features between the helix and fan structures.

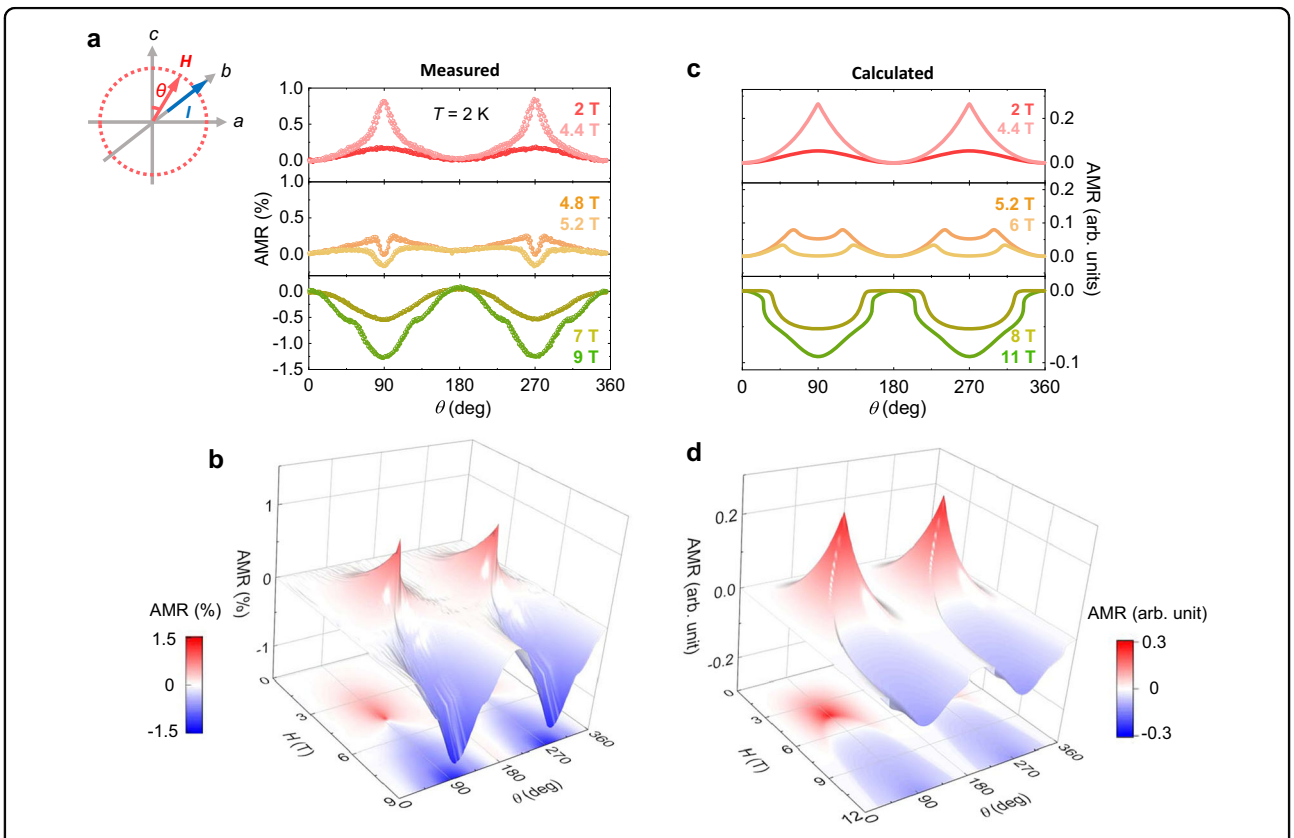

Fig. 4 Experimental and theoretical anisotropic magnetoresistance. a Plots of AMR (%) measured at $T = 2$ K by rotating $H = 2$, 4.4, 4.8, 5.2, 7, and 9 T in the ac plane with current along the b-axis, I // b. The geometry of AMR measurement is schematically presented. $\theta = 0°$ for the c-axis and $\theta = 90°$ for the a-axis. **b** Contour plots of AMR at $T = 2$ K. **c** Plots of calculated AMR data at $H = 2$, 4.4, 5.2, 6, 8, and 11 T. **d** Contour plots of AMR obtained from theoretical estimations.

Discussion

In this study, we have demonstrated a mechanism to generate the sign-changing AMR phenomenon that originates from electrically distinctive dual magnetic phases separated by a magnetic phase transition. The magnetic transition emerges from the competition of diverse energy scales included in the model Hamiltonian. Specifically, the highly 2D characteristic of magnetocrystalline anisotropy is vital for determining the consistency between bulk measurements and theoretical calculations. In pursuance of the AMR effect predominantly caused by the magnetocrystalline anisotropy in AFM spintronics, the approach proposed in this study is applicable to a variety of antiferromagnets in which the distinct features of the anisotropic magnetotransport could be observed depending on the alteration of the magnetocrystalline anisotropy. The development of magnetic devices with the desired properties requires detectable macroscopic effects that are contingent on the variable magnetic states. In complex noncollinear antiferromagnets, more spintronic effects can exist. Therefore, the electrical access to various AFM memory states associated with the evolution of helical spin texture would provide an opportunity for realizing multilevel AFM memory devices.

Notably, the reversal phenomenon of AMR has seldom been reported. In a previous study on ferromagnetic $La_{0.7}Ca_{0.3}MnO_3$ ultrathin films, a sign reversal of the AMR originated from the planar tensile strain that facilitated the rotation of the ferromagnetic easy axis, which is different from the present case[37]. The sign-tunable AMR effect in a single-phase noncollinear antiferromagnet is unique owing to its intrinsic origin from the electrically discernible magnetic phases. Additionally, a variety of topological states mediated by spin-orbit interactions yield exotic topological magnetism[38–40]. More recently, helical magnetism driven by Weyl-mediated RKKY interactions was observed in a Weyl semimetal, NdAlSi[41]. The recognition of versatile AFM memory states in a helimagnet offers valuable guidelines for investigating the intimate interplay between the electronic and magnetic topological properties and thus for implementing topological AFM spintronics.

In summary, we propose a new single-crystalline spintronic material in which the sign-tunable AMR effect reflects completely intrinsic bulk properties. These results are beneficial for the development of AFM spintronics, which has been driven by novel materials. Theoretically, the highly anisotropic 2D spin characteristic was highlighted as a core factor for anisotropic magnetotransport in a natural noncollinear AFM ECA. The scheme followed in this study is a particular type of spin-reorientation-driven mechanism to study the intriguing anisotropic properties, which can motivate further investigations of noncollinear AFM for extensive spintronic applications.

Acknowledgements
This work was supported by the National Research Foundation of Korea (NRF) through grants 2016R1D1A1B01013756, NRF-2017R1A5A1014862 (SRC program: vdWMRC center), NRF-2021R1A2C1006375, and NRF-2022R1A2C1006740. We would like to thank Editage (www.editage.co.kr) for English language editing.

Author contributions
N.L. and Y.J.C. conceived the study. J.H.K. and J.M.H. synthesized the single crystals. J.H.K., H.J.S., J.M. H, K.W.J., and J.S.K. measured the physical properties of the crystals. J.H.K. and H.J.S. acquired the STEM images. M.K.K. and K.M. performed the theoretical calculations. J.H.K., H.J.S., M.K.K., K.M., N.L., and Y.J.C. analyzed the data and prepared the manuscript. All authors have read and approved the final version of the manuscript.

Conflict of interest
The authors declare no competing interests.

Supplementary information The online version contains supplementary material available at https://doi.org/10.1038/s41427-022-00415-2.

Received: 21 March 2022 Revised: 15 June 2022 Accepted: 17 June 2022.
Published online: 5 August 2022

References

1. Baltz, V. et al. Antiferromagnetic spintronics. *Rev. Mod. Phys.* **90**, 015005 (2018).
2. Jungwirth, T. et al. The multiple directions of antiferromagnetic spintronics. *Nat. Phys.* **14**, 200–203 (2018).
3. Jungfleisch, M. B., Zhang, W. & Hoffmann, A. Perspectives of antiferromagnetic spintronics. *Phys. Lett. A* **382**, 865–871 (2018).
4. Godinho, J. et al. Electrically induced and detected Néel vector reversal in a collinear antiferromagnet. *Nat. Commun.* **9**, 4686 (2018).
5. Jungwirth, T., Marti, X., Wadley, P. & Wunderlich, J. Antiferromagnetic spintronics. *Nat. Nanotechnol.* **11**, 231–241 (2016).
6. Wadley, P. et al. Tetragonal phase of epitaxial room-temperature antiferromagnet CuMnAs. *Nat. Commun.* **4**, 2322 (2013).
7. Liu, Z. Q. et al. Electrical switching of the topological anomalous Hall effect in a non-collinear antiferromagnet above room temperature. *Nat. Electron.* **1**, 172–177 (2018).
8. Železný, J., Zhang, Y., Felser, C. & Yan, B. Spin-Polarized Current in Noncollinear Antiferromagnets. *Phys. Rev. Lett.* **119**, 187204 (2017).
9. Nan, T. et al. Controlling spin current polarization through non-collinear antiferromagnetism. *Nat. Commun.* **11**, 4671 (2020).
10. Chen, T. et al. Anomalous transport due to Weyl fermions in the chiral antiferromagnets Mn_3X, X = Sn, Ge. *Nat. Commun.* **12**, 572 (2021).
11. Nakatsuji, S., Kiyohara, N. & Higo, T. Large anomalous Hall effect in a non-collinear antiferromagnet at room temperature. *Nature* **527**, 212–215 (2015).
12. Nayak, A. K. et al. Large anomalous Hall effect driven by a nonvanishing Berry curvature in the noncolinear antiferromagnet Mn_3Ge. *Sci. Adv.* **2**, e1501870 (2016).
13. Matsuda, T. et al. Room-temperature terahertz anomalous Hall effect in Weyl antiferromagnet Mn_3Sn thin films. *Nat. Commun.* **11**, 909 (2020).
14. Finco, A. et al. Imaging non-collinear antiferromagnetic textures via single spin relaxometry. *Nat. Commun.* **12**, 767 (2021).
15. Reichlova, H. et al. Imaging and writing magnetic domains in the non-collinear antiferromagnet Mn_3Sn. *Nat. Commun.* **10**, 5459 (2019).
16. Higo, T. et al. Large magneto-optical Kerr effect and imaging of magnetic octupole domains in an antiferromagnetic metal. *Nat. Photonics* **12**, 73–78 (2018).
17. Wang, H. et al. Giant anisotropic magnetoresistance and nonvolatile memory in canted antiferromagnet Sr_2IrO_4. *Nat. Commun.* **10**, 2280 (2019).
18. Song, C. et al. How to manipulate magnetic states of antiferromagnets. *Nanotechnology* **29**, 112001 (2018).

19. O'Grady, K. et al. Anisotropy in antiferromagnets. *J. Appl. Phys.* **128**, 040901 (2020).
20. Lee, N. et al. Antiferromagnet-based spintronic functionality by controlling isospin domains in a layered perovskite iridate. *Adv. Mater.* **30**, 1805564 (2018).
21. Wang, C. et al. Anisotropic magnetoresistance in antiferromagnetic Sr_2IrO_4. *Phys. Rev. X* **4**, 041034 (2014).
22. Marti, X. et al. Room-temperature antiferromagnetic memory resistor. *Nat. Mater.* **13**, 367–374 (2014).
23. Zeng, F. L. et al. Intrinsic mechanism for anisotropic magnetoresistance and experimental confirmation in Co_xFe_{1-x} single-crystal films. *Phys. Rev. Lett.* **125**, 097201 (2020).
24. Fina, I. et al. Anisotropic magnetoresistance in an antiferromagnetic semiconductor. *Nat. Commun.* **5**, 4671 (2014).
25. Park, B. G. et al. A spin-valve-like magnetoresistance of an antiferromagnet-based tunnel junction. *Nat. Mater.* **10**, 347–351 (2011).
26. Uchida, M., Onose, Y., Matsui, Y. & Tokura, Y. Real-space observation of helical spin order. *Science* **311**, 359–361 (2006).
27. Takeuchi, Y. et al. Chiral-spin rotation of non-collinear antiferromagnet by spin–orbit torque. *Nat. Mater.* **20**, 1364–1370 (2021).
28. Keffer, F. & Kittel, C. Theory of antiferromagnetic resonance. *Phys. Rev.* **85**, 329–337 (1952).
29. Olejník, K. et al. Terahertz electrical writing speed in anantiferromagnetic memory. *Sci. Adv.* **4**, eaar3566 (2018).
30. Sangeetha, N. S. et al. Enhanced moments of Eu in single crystals of the metallic helical antiferromagnet $EuCo_{2-y}As_2$. *Phys. Rev. B* **97**, 144403 (2018).
31. Johnston, D. C. Magnetic structure and magnetization of helical antiferromagnets in high magnetic fields perpendicular to the helix axis at zero temperature. *Phys. Rev. B* **96**, 104405 (2017).
32. Tan, X. et al. A transition from localized to strongly correlated electron behavior and mixed valence driven by physical or chemical pressure in ACo_2As_2 (A = Eu and Ca). *J. Am. Chem. Soc.* **138**, 2724–2731 (2016).
33. Ding, Q. P., Higa, N., Sangeetha, N. S., Johnston, D. C. & Furukawa, Y. NMR determination of an incommensurate helical antiferromagnetic structure in $EuCo_2As_2$. *Phys. Rev. B* **95**, 184404 (2017).
34. Blundell, S. Magnetism in Condensed Matter. (Oxford University Press, 2003).
35. Takeuchi, T. et al. Magnetization process in $EuCo_2P_2$ and EuT_2Ge_2 (T: transition metal): comparison of experiment and theory. *J. Phys. Soc. Jpn.* **90**, 034709 (2021).
36. Ballinger, J., Wenger, L. E., Vohra, Y. K. & Sefat, A. S. Magnetic properties of single crystal $EuCo_2As_2$. *J. Appl. Phys.* **111**, 07E106 (2012).
37. Sharma, H., Tulapurkar, A. & Tomy, C. V. Sign reversal of anisotropic magnetoresistance in $La_{0.7}Ca_{0.3}MnO_3/SrTiO_3$ ultrathin films. *Appl. Phys. Lett.* **105**, 222406 (2014).
38. Šmejkal, L., Mokrousov, Y., Yan, B. & MacDonald, A. H. Topological antiferromagnetic spintronics. *Nat. Phys.* **14**, 242–251 (2018).
39. Yin, J.-X. et al. Quantum-limit Chern topological magnetism in $TbMn_6Sn_6$. *Nature* **583**, 533–536 (2020).
40. Yin, J.-X. et al. Spin-orbit quantum impurity in a topological magnet. *Nat. Commun.* **11**, 4415 (2020).
41. Gaudet, J. et al. Weyl-mediated helical magnetism in NdAlSi. *Nat. Mater.* **20**, 1650–1656 (2021).